



Acoustic properties across the human skull

Thomas S. Riis, Taylor D. Webb, Jan Kubanek*

Department of Biomedical Engineering, University of Utah, Salt Lake City, 84112, UT, United States

ARTICLE INFO

MSC:
0000
1111

Keywords:

Transcranial ultrasound
Skull
Transmission
Attenuation
Phase
Thickness

ABSTRACT

Transcranial ultrasound is emerging as a noninvasive tool for targeted treatments of brain disorders. Transcranial ultrasound has been used for remotely mediated surgeries, transient opening of the blood–brain barrier, local drug delivery, and neuromodulation. However, all applications have been limited by the severe attenuation and phase distortion of ultrasound by the skull. Here, we characterized the dependence of the aberrations on specific anatomical segments of the skull. In particular, we measured ultrasound propagation properties throughout the perimeter of intact human skulls at 500 kHz. We found that the parietal bone provides substantially higher transmission (average pressure transmission $31 \pm 7\%$) and smaller phase distortion (242 ± 44 degrees) than frontal ($13 \pm 2\%$, 425 ± 47 degrees) and occipital bone regions ($16 \pm 4\%$, 416 ± 35 degrees). In addition, we found that across skull regions, transmission strongly anti-correlated ($R = -0.79$) and phase distortion correlated ($R = 0.85$) with skull thickness. This information guides the design, positioning, and skull correction functionality of next-generation devices for effective, safe, and reproducible transcranial focused ultrasound therapies.

1. Introduction

Transcranial focused ultrasound offers incisionless and targeted treatment options for disorders of brain function [1–3]. At high intensities, ultrasound has been used to lesion malfunctioning or diseased deep brain targets [4,5]. At low intensities, ultrasound can be used to deliver large drugs, genes, or stem cells across the blood–brain barrier [6–9]; release drugs in specific brain regions without affecting the blood–brain barrier [10–13]; and to modulate neural activity in a transient [14–17] or sustained [18–25] fashion.

The clinical utility of these applications has been impeded by the severe aberrations of ultrasound by the human skull. In the surgical applications, the highly variable attenuation and phase distortions can leave a substantial proportion of patients untreated [26]. The skull aberrations have limited the predictability of the ultrasound magnitude delivered into target [27] and so have also impeded the translation of low-intensity applications. A tight control of the delivered dose is particularly important for ultrasound-mediated opening of the blood–brain barrier, in which small changes in the ultrasound pressure at target – on the order of 10–20% – can lead to vast differences in the scale of the blood–brain barrier disruption [6,28]. The skull aberrations have also curbed effective and reproducible applications of ultrasonic neuromodulation [29,30] and local drug release, which require a well-defined ultrasound dose [11,31].

To maximize ultrasound penetration through the skull and to maximize the predictability of the delivered dose, ultrasound should be

applied through skull segments that cause the least amount of attenuation and phase distortion. In diagnostic applications, small imaging probes can be applied through the temporal window, which has a relatively low ultrasound attenuation [32–36]. However, therapeutic applications often require large apertures or arrays with many elements for focal delivery of considerable amount of energy [4,18,19,29,37–40]. Any future design that maximizes ultrasound penetration and the predictability of the delivered dose should take into account the dependence of the aberrations on specific anatomical regions of the skull.

This information is currently incomplete. Existing studies have provided insights into inter-subject variability of acoustic properties [32, 41–44], estimates of average attenuation and phase distortions [32,41–50], as well as approaches on how these aberrations may be compensated for [4,51–57]. However, acoustic measurements have only been provided for discrete sets of chosen samples or skull flaps [32,41–45]. Consequently, there is no systematic assessment of acoustic propagation properties within single intact skulls as a function of anatomical location.

To address this, we devised a setup that allowed us to measure ultrasound propagation properties throughout the perimeter of intact human skulls. We complemented these acoustic measurements with caliper measurement of the corresponding skull thickness. The resulting data quantify the transmission and phase distortion through anatomically

* Corresponding author.

E-mail addresses: tom.riis@utah.edu (T.S. Riis), taylor.webb@utah.edu (T.D. Webb), jan.kubanek@utah.edu (J. Kubanek).

defined segments of the skull, and show how these variables depend on the skull thickness. This information guides the design and placement of future devices for effective applications of transcranial ultrasound in the clinics.

2. Materials and methods

2.1. Subjects

Three *ex-vivo* skulls were used in this study (Skull 1: male, 84 years; Skull 2: male, 61 years; Skull 3: female 68 years). The skulls were obtained under a research agreement from Skulls Unlimited (Oklahoma City, OK). An opening was made at the bottom of each skull to enable skull rotation around a receiving transducer positioned inside the skull.

Each skull was degassed overnight in a deionized water. Degassing is a standard procedure that removes trapped air in the porous cancellous bone which is filled with blood and fat *in-vivo* [41,50,58–60]. Following the degassing, the skull was transferred, within the degassed water, into an experimental tank filled with continuously degassed water (AIMS III system with AQUAS-10 Water Conditioner, Onda). The water conditioner (AQUAS-10) treats water for ultrasound measurements in compliance with IEC 62781. The conditioner degasses water to remove undesired bubbles, removes suspended particles and biological contaminants, and deionizes water. The dissolved oxygen is between 2.0–2.5 PPM during continuous operation, according to measurements provided by the manufacturer (Onda). In comparison, tap water contains about 10.5 PPM of dissolved oxygen.

The skull was held in place by a pair of thin neodymium rare earth magnets (550lbs lift, 2.5-inch diameter, Neosmuk), one positioned below the skull and one above, at the center of the sagittal suture. The magnets allowed us to firmly hold and rotate each skull without having to perturb its surface.

2.2. Coordinates

Prior to degassing, the through-transmit plane was established using 4 markers that were chosen such as to avoid frontal and sphenoidal sinuses and to maintain perpendicular ultrasound propagation. Specifically, a frontal marker was positioned 49 mm above the center of the nasion. Two parietal markers, one on the left and one on the right, were made 17 mm above the squamous suture and at the widest point of the skull. The final, occipital marker was made approximately 17 mm above the center of theinion. An angular positioner assembly (AP02-S, Onda) was aligned with the 4 markers in the following way: the frontal marker corresponded to 0 degrees, the right parietal marker to 90 degrees, the occipital marker to 180 degrees, and the left parietal marker to 270 degrees (Fig. 1b).

2.3. Skull thickness measurements

To measure skull thickness, the 4 markers were connected with a line. A precision caliper gage (Fowler 54-554-630, 0.1 mm accuracy) was used to measure the thickness of the skull in 3 mm steps. Each measurement was repeated 3 times after fully retracting and re-positioning the caliper in each measurement to gauge non uniformity of the skull section thickness; the resulting values were averaged together. Only rarely was there a difference of more than 0.1 mm between the 3 measurements. The standard deviation of all measurements was 0.07 mm. The thickness measurements may have incurred additional error due to the imperfect alignment between the outer and inner surface and the natural curvature of the skull. Such errors were assumed to be minimal as in previous studies [49,61].

2.4. Through-transmit setup

Two transducers operating at 500 kHz center frequency (V301-SU, Olympus, unfocused, 28.5 mm face diameter) were mounted to a breadboard such that they faced each other. One transducer served as a transmitter and one as a receiver. The distance between the transducers' faces was 100 mm. The breadboard with the mounted transducers was positioned at the bottom of the water tank. The center of each face of the transducer was 145 mm above the breadboard. Each skull was electronically translated and rotated such that (1) the line connecting the centers of the two transducers intersected with the 4 markers (2) all segments of the skull were in the far field of the transmitting transducer (at a distance greater than 68.6 mm). The beam width of our unfocused transducer at the skull was calculated as: $FWHM = 0.704 \lambda z/a = 10$ mm, where λ is wavelength, z is axial distance from the transducer face, and a is radius of the transducer. Across this length, the deviation in skull thickness is considered negligible [61]. The acoustic pathway connecting the centers of the two transducers was determined using a custom 3D printed plastic pointer positioned into the holder of the transmitting transducer. We used 3D CT images of the skull to measure the incident angles for each measured skull segment. The incident angle was taken as the angle between the acoustic path and the normal vector of the skull surface at that point. The mean+SD incidence angle was 7.3+4.9 degrees. Incidence angles within this range have only minimal impact on the measurements and do not affect our conclusions [41].

2.5. Ultrasound system and pulses

The through-transmit protocol was implemented on the Vantage256 system (Verasonics), using a custom matlab script. We used chirp pulses of 3 distinct forms. Chirps are frequency-modulated waveforms that have a narrow autocorrelation function. A narrow autocorrelation function maximizes the accuracy of the detection of time delays in through-transmit procedures [62,63]. Chirp3 consisted of three consecutive cycles of [0.75, 1, 1.25] times the center frequency of 500 kHz. Chirp4 consisted of four consecutive cycles with [0.75, 1, 1.25, 1.5] times the center frequency. Chirp5 consisted of five consecutive cycles with [0.5, 0.75, 1, 1.25, 1.5] times the center frequency. Our transducers were broadband (Videoscan series, Olympus) and so capable of emitting the frequency spectrum. Each pulse was transmitted and detected 32 times; the responses were averaged together.

2.6. Through-transmit procedure

The through-transmit procedure quantifies the changes in amplitudes and received times following an introduction of an object (e.g., skull) into the transmit–receive path. Data were first collected in water. This provided an average no-skull receive waveform. Consequently, the skull was lowered into a location described above, and gradually rotated in 1 degree increments, with the through-transmit data taken at each. This provided through-skull receive waveforms. The maximum of each through-skull receive waveform divided by the maximum of the no-skull receive waveform provided the relative pressure transmission, separately for each angle (Fig. 3, Fig. 5). To determine the time shift, a cross-correlation was computed between the no-skull and through-skull receive waveforms, separately for each angle. The peak of the cross-correlation defined the time shift. This time corresponds to the speedup values shown in Fig. 6 and Fig. 7. The three pulses produced equivalent values of time shift in most cases. These values were averaged together.

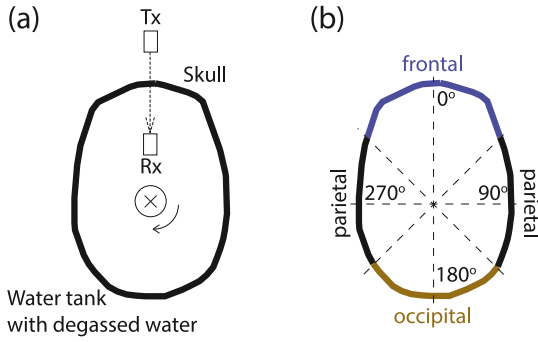


Fig. 1. Through-transmit measurements across intact skulls. (a) Top view of the setup. Degassed and hydrated *ex-vivo* skulls were held by a robotic arm and were secured to the skull using two opposing magnets positioned at the center of the sagittal suture (the thin circle shows the position of the magnets). This robotic arm, connected to the magnet at the top of the skull, allowed us to electronically rotate the skull and so collect through-transmit measurements over individual segments of the skull within the imaging plane. The through-transmit measurements were achieved using a transmitting (Tx) and a receiving (Rx) transducer facing each other at a distance of 100 mm. The direction of ultrasound transmission is indicated by the dashed arrow. The through-transmit measurements were acquired at each rotation step of 1 degree. (b) Parameterization of the skull bone into parietal (45–135 and 225–315 degrees), occipital (135–225 degrees), and frontal (315–45 degrees) regions.

2.7. Through-transmit relationships

The ultrasound speedup through a skull segment τ is mathematically proportional to the thickness of the segment h through:

$$\tau = h \left(\frac{1}{c_w} - \frac{1}{c_s} \right),$$

where $c_w = 1481$ m/s is the speed of sound through water, and c_s is the average speed of sound through the skull segment. The phase distortion or shift caused by the speedup is equal to $\omega\tau$, where ω is the angular frequency.

The measured pressure transmission (T) depends on ultrasound reflection from the individual layers of the skull and on a set of attenuation factors (α) that include ultrasound absorption and scattering. Under an assumption that these factors can be considered separate and independent, we can write:

$$T = R \exp(-\alpha h),$$

where R is the loss due to reflection and h is the skull segment thickness. Taking a logarithm of this equation yields:

$$\ln T = \ln(R) - \alpha h.$$

The set of thickness-dependent attenuation factors α can be inferred as a slope of the relationship between $\ln(T)$ and h (Fig. 5).

3. Results

We assessed the acoustic properties across intact *ex-vivo* human skulls using an apparatus that allowed controlled rotation about a central axis (Fig. 1). The acoustic properties were characterized using standard through-transmit measurements (Materials and Methods), with the transmitting/receiving transducer positioned outside/inside of the skull. The position of the two transducers was fixed; only the skull was rotated. The through-transmit values obtained through the skull were compared to free-field values in which no skull was present, as in previous studies [41,55].

We performed the through-transmit measurements in three degassed and hydrated *ex-vivo* skulls. The CT images of the skulls within the through-transmit plane are shown in Fig. 2.

The relative pressure transmission across the individual anatomical locations is shown in (Fig. 3). The figure reveals that the highest

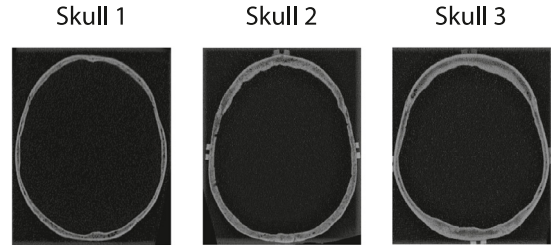


Fig. 2. Subjects. CT scans for the three *ex-vivo* skulls used in this study. The images were taken at the through-transmit plane.

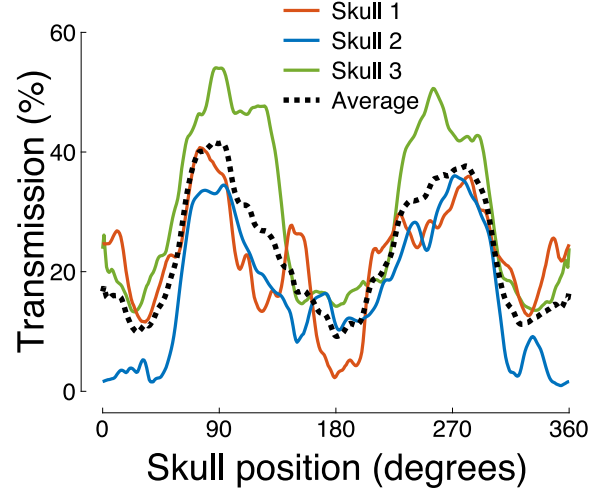


Fig. 3. Ultrasound transmission throughout the skull. The figure shows the relative pressure attenuation (skull versus no skull) for each measured segment of the skull. The carrier frequency was 500 kHz.

Table 1
Acoustic properties quantified over distinct skull regions..

	T (%)		τ (μ s)		h (mm)		c_s (m/s)	
	Mean	SD	Mean	SD	Mean	SD	Mean	SD
Frontal	13.2	1.9	2.4	0.3	7.3	0.6	2871	289
Parietal	31.2	7.3	1.3	0.2	5.1	0.6	2486	193
Par. optimum	41.6	9.4	1.1	0.4	4.3	0.6		
Occipital	15.8	4.4	2.3	0.2	8.5	1.4	2603	160
All	22.9	10.2	1.8	0.6	6.5	1.7	2609	266

The table lists the mean \pm SD transmission (T), speedup (τ), thickness (h), and speed of sound (c_s) as a function of skull position (rows). The parietal optimum entry lists maximal transmission, minimal speedup, and minimal thickness, averaged across the 3 skulls.

transmission was observed in segments centered over the parietal bone. The average transmission in the parietal regions was 2.4 higher than in the temporal regions and 2.0 higher than in the occipital regions (Table 1). The transmission was maximal within the parietal bone and delivered an average 41.6% of the ultrasound pressure across the three skulls. As apparent from the figure, the transmission varied substantially across the 3 subjects—the 3 skulls showed an average 22.2%, 16.8%, and 29.5% transmission, respectively. Effects of the skull position and subject were both significant. In particular, a two-way ANOVA revealed a significant modulation of the pressure transmission by the skull position ($F(360, 720) = 7.48$, $p = 4.7 \times 10^{-115}$) and by subject ($F(2, 720) = 353.90$, $p = 9.1 \times 10^{-108}$).

We measured the thickness of the skulls across the through-transmit plane using a caliper (see Materials and Methods). The skull thickness as a function of position is shown in Fig. 4. The figure reveals a substantial variability in skull thickness within and across individuals. The thickness ranged from 3.1 mm to 14.0 mm, with an average of

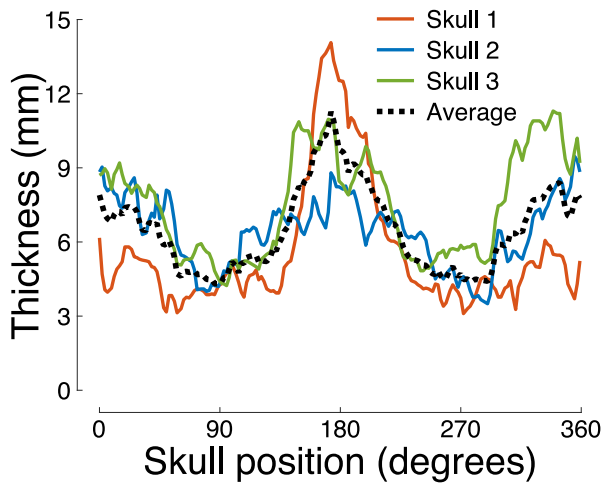


Fig. 4. Skull thickness across angular position. Mean thickness of each segment of the skull within the through-transmit plane. Three independent measurements were taken at each position.

6.5 mm and a standard deviation of 1.7 mm. The parietal bone was on average thinner than the frontal and occipital bones (Table 1). The thickness varied across the 3 subjects, with average values of 5.6 mm, 6.4 mm, and 7.5 mm, respectively. A two-way ANOVA revealed a significant modulation of thickness by the skull position ($F(66, 332) = 3.75$, $p = 7.2 \times 10^{-25}$) and by subject ($F(2, 332) = 64.96$, $p = 1.6 \times 10^{-24}$).

The profiles of pressure transmission (Fig. 3) and skull thickness (Fig. 4) suggest an inverse relationship between these quantities: the thinner the skull, the more effective the transmission. Indeed, we found that skull thickness is a strong predictor of the transmission efficacy (Fig. 5). In the three skulls, skull thickness explained 45%, 65%, and 81% of the variance in the pressure transmission, respectively. An ANCOVA model, with a continuous factor of skull thickness and a discrete factor of subject, found a significant effect of thickness ($F(1, 495) = 974.45$, $p = 4.9 \times 10^{-119}$) as well as an effect of subject ($F(2, 495) = 161.15$, $p = 1.3 \times 10^{-54}$) and thickness \times subject interaction ($F(2, 495) = 90.31$, $p = 3.7 \times 10^{-34}$). Thus, there is a significant difference in the pressure transmission across the subjects, and the dependence of transmission on skull thickness is subject-specific. We further investigated the thickness dependence of the natural logarithm of the pressure transmission. The logarithmic formulation may enable the quantification of skull thickness-dependent attenuation factors α from the slope of the linear relationships showed in the bottom part of Fig. 5 (see Materials and Methods). The slopes for the 3 skulls were -0.176 , -0.489 , and -0.208 , respectively. According to the simple—though likely simplistic—model (Materials and Methods), this slope translates into thickness-dependent attenuation factors of $\alpha = 176$ Np/m, $\alpha = 489$ Np/m, and $\alpha = 208$ Np/m, respectively.

It is known that the skull speeds up the propagation of ultrasound compared to water. This relative speedup leads to distortions or shifts of the ultrasound phase. We investigated how this speedup and phase distortion depend on the individual segments of the skull. We found that the distortion was smallest for the parietal regions (Fig. 6), with a value 1.8 times smaller than for the frontal and 1.7 times smaller than the occipital regions (Table 1). A two-way ANOVA revealed a significant modulation of the phase distortion by the skull position ($F(360, 654) = 5.08$, $p = 1.5 \times 10^{-72}$) and by subject ($F(2, 654) = 694.63$, $p = 1.7 \times 10^{-162}$).

The speedup and the associated phase distortion should be linearly proportional to skull thickness (see Materials and Methods). This proportionality has been demonstrated previously [49]. Indeed, we confirmed these findings (Fig. 7). In the 3 skulls, skull thickness explained 73%, 78%, and 81% of the variance in the phase aberration,

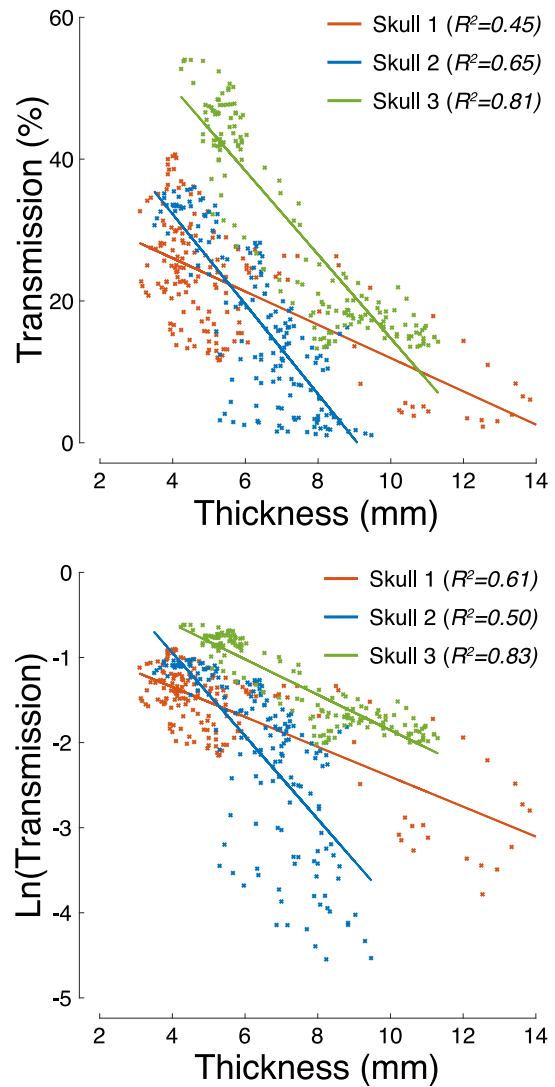


Fig. 5. Ultrasound transmission is strongly governed by skull thickness. Ultrasound pressure transmission (top) and its natural logarithm (bottom) as a function of skull thickness. The R^2 values listed in the inset provide the amount of variance explained by the linear fits superimposed on the plots.

respectively. An ANCOVA model, again with a continuous factor of thickness and a discrete factor of subject, found a significant effect of thickness ($F(1, 464) = 1175.53$, $p = 2.9 \times 10^{-129}$) as well as an effect of subject ($F(2, 464) = 55.92$, $p = 1.7 \times 10^{-22}$) and thickness \times subject interaction ($F(2, 464) = 142.78$, $p = 4.8 \times 10^{-49}$). Thus, the linear relationship between the phase aberration and skull thickness, albeit robust within an individual, is variable across individuals.

The previous finding suggests an appreciable difference in the average speed of sound across the skulls. We investigated the speed of sound across the skulls and across the individual segments of each skull (Fig. 8). There was a substantial variability in the speed of sound, both across and within the subjects. In particular, the three skulls showed a mean \pm SD of 2451 ± 383 m/s, 2401 ± 307 m/s, and 2887 ± 412 m/s, respectively. Although there was a trend for the speed of sound to be lower for the parietal bone (Table 1) compared to frontal and occipital bone, this was not consistent across subjects (Fig. 8). A two-way ANOVA confirmed the significant variability of the speed of sound by skull position ($F(359, 652) = 1.29$, $p = 0.0024$) and by subject ($F(2, 652) = 173.07$, $p = 5.1 \times 10^{-61}$).

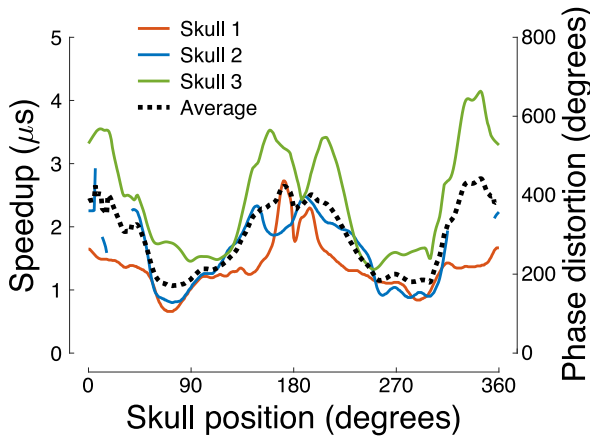


Fig. 6. Speedup and phase distortion across the skull. Ultrasound speedup through the skull (τ) and the associated phase distortion ($\omega\tau$) as a function of the skull position. Several segments of the occipital and frontal bones in Skull 2 provided extreme aberration, rendering the through-transmit cross-correlation unreliable; values for these segments are therefore not shown.

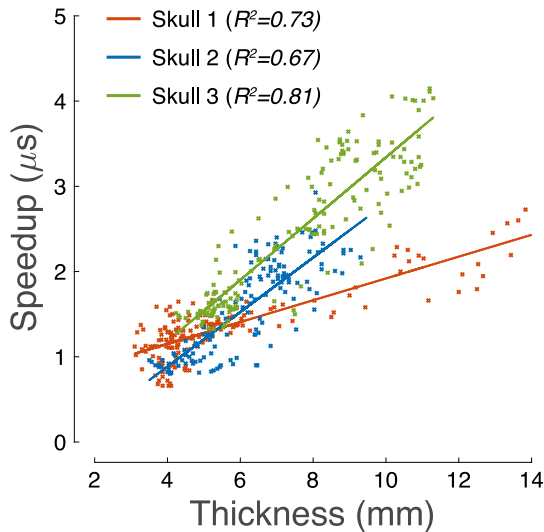


Fig. 7. Ultrasound phase distortion is proportional to skull thickness. Ultrasound speedup through individual segments of the skull as a function of skull thickness. The R^2 values listed in the inset provide the amount of variance explained by the linear fits superimposed on the plots.

4. Discussion

In this study, we investigated the transmission and phase distortion of ultrasound across intact human skulls.

We found that 500 kHz ultrasound—a common frequency for transcranial applications in humans—was most effectively transmitted through segments of the parietal bone (Fig. 3), in all three *ex-vivo* specimens. We further found that the transmission was strongly dependent on the skull thickness: the thinner the skull, the more effective the transmission (Fig. 5). Since parietal bone was found to be the thinnest on average (Fig. 4, Table 1), this negative correlation can partially explain the facilitated transmission through the parietal bone.

A negative correlation between skull thickness and ultrasound transmission could be expected, but has not, to our knowledge, been shown explicitly. Our direct measurements of skull thickness using a caliper uncovered a surprisingly tight relationship (64% of variance explained, mean across 3 skulls) between the skull thickness and ultrasound transmission. However, the slopes of the dependence on the thickness

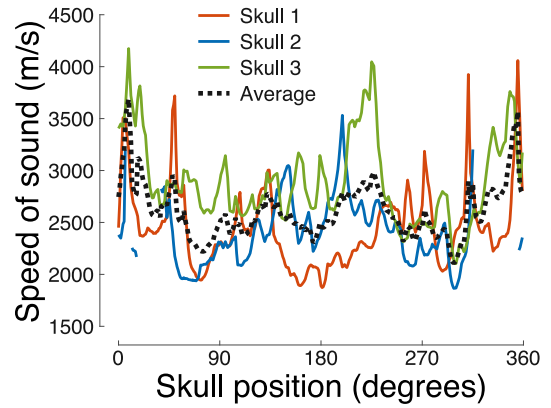


Fig. 8. Speed of sound across the skull. The speed of sound (c_s) determined from the through-transmit τ values (see Materials and Methods) as a function of the skull position.

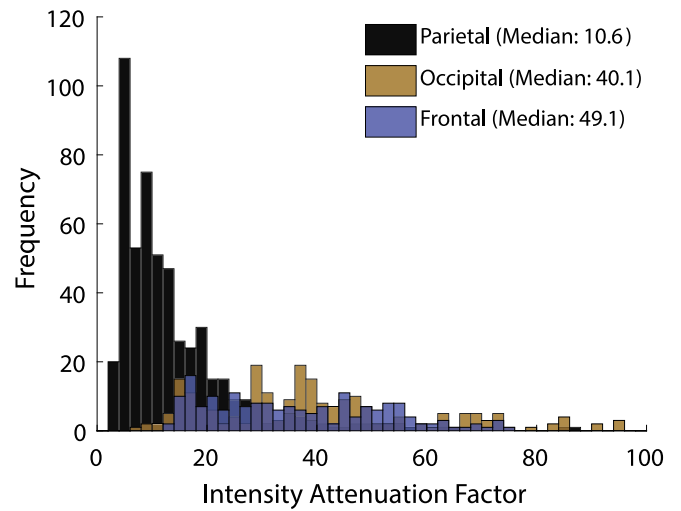


Fig. 9. Intensity attenuation factor distribution by skull section. Intensity attenuation factor (T^{-2}) varies significantly by region of the skull. The parietal bone's 5th to 95th percentile range is an order of magnitude lower than both the frontal and occipital regions.

varied across the 3 skulls. In addition—and as observed in previous studies [41,43,44]—we found a significant difference in the average transmission across the 3 skulls. These subject-specific factors complicate a parsimonious description of ultrasound transmission based on skull thickness alone.

We found that the speedup of ultrasound due to the propagation through the skull bone, and the associated phase distortion, are also smallest over parietal bone segments (Fig. 6). This finding can be explained by our (Fig. 7) and previous [49] findings that the speedup and phase shift are proportional to skull thickness. The slope of this dependence, which is a function of the average speed of sound through the skull (see Materials and Methods), varied significantly across the skulls. This variability has been observed also in previous studies, but can be accounted for using CT skull density measurements [55,64].

The data provided in this study corroborate the notion of substantial variability of acoustic properties across individuals [32,41–44]. In addition to the inter-subject variability, we have shown, in a systematic experiment, that there is substantial skull location-dependent variability. Transmission and phase shift comprised a well-defined function of skull location (Fig. 3, Fig. 6). The speed of sound, in contrast, showed a much less predictable pattern (Fig. 8).

The primary goal of our study was to identify the regions of the skull that provide optimal transmission. Although our robotic system

allowed us to assess the acoustic properties across the perimeter of the skull, it only enabled us to operate along the middle segments of the skull. Acoustic properties for more dorsal portion of calvariae are to be found elsewhere [42,43]. In addition, degassed ex-vivo skulls show somewhat larger attenuation than freshly excised skulls [41]. The values presented in this study should be taken as relative—with respect to anatomical location or skull thickness, rather than absolute. While our subjects were limited to people of relatively old age, no significant correlation has been found between age and bone density, dipole thickness, or cranial vault thickness [65–67].

The thickness measurements revealed a surprisingly tight relationship between ultrasound transmission and skull thickness. The correlation between skull thickness and ultrasound transmission may be even higher if we did not assume a uniform thickness of the skull portion intersecting each measured beam, i.e., if the caliper measurements were performed across the entire skull. This relationship invites future investigations with the goal to account for the attenuation of ultrasound transmission through the skull based on CT [68], MRI [68,69], or other imaging modalities [57].

The importance of selecting appropriate sonication path through the skull is highlighted in Fig. 9, which shows the distribution of intensity attenuation through parietal, frontal, and occipital segments across all three skulls. The figure demonstrates that sonicating the same target through different sections of the skull could deliver intensities that differ by an order of magnitude if this factor is not accounted for. Moreover, the figure reveals the amount of variability in the intensity attenuation across the individual skull segments. Applying ultrasound through occipital or frontal parts of the skull makes the dose delivered into a target essentially unpredictable. The variability is much smaller when ultrasound is delivered through the parietal bone, increasing the operator's confidence in the delivered dose.

In summary, we measured the acoustic properties throughout the perimeter of intact human ex-vivo skulls. We found that regions of the parietal bone provide much more effective transmission and lower phase distortion than frontal and occipital regions. We further found that the ultrasound transmission strongly depends on the skull thickness. These data inform future approaches to compensate for ultrasound skull aberrations and guide the design of future devices for safe, effective, and reproducible transcranial ultrasound therapies.

Acknowledgment

This work was supported by the National Institutes of Health, United States (grants R00NS100986 and F32MH123019).

References

- [1] K. Hynynen, F.A. Jolesz, Demonstration of potential noninvasive ultrasound brain therapy through an intact skull, *Ultrasound Med. Biol.* 24 (2) (1998) 275–283.
- [2] E. Landhuis, Ultrasound for the brain, *Nature* 551 (7679) (2017) 257–259.
- [3] Y. Meng, K. Hynynen, N. Lipsman, Applications of focused ultrasound in the brain: From thermoablation to drug delivery, *Nat. Rev. Neurol.* (2020) 1–16.
- [4] P. Ghanouni, K.B. Pauly, W.J. Elias, J. Henderson, J. Sheehan, S. Monteith, M. Wintermark, Transcranial MRI-guided focused ultrasound: a review of the technologic and neurologic applications, *Am. J. Roentgenol* 205 (1) (2015) 150–159.
- [5] M. Giordano, V.M. Caccavella, I. Zaed, L.F. Manzillo, N. Montano, A. Olivi, F.M. Polli, Comparison between deep brain stimulation and magnetic resonance-guided focused ultrasound in the treatment of essential tremor: a systematic review and pooled analysis of functional outcomes, *J. Neurol. Neurosurg. Psychiatry* 91 (12) (2020) 1270–1278.
- [6] A. Carpentier, M. Canney, A. Vignot, V. Reina, K. Beccaria, C. Horodyckid, C. Karachi, D. Leclercq, C. Lafon, J.-Y. Chapelon, et al., Clinical trial of blood-brain barrier disruption by pulsed ultrasound, *Sci. Transl. Med.* 8 (343) (2016) 343.
- [7] N. Lipsman, Y. Meng, A.J. Bethune, Y. Huang, B. Lam, M. Masellis, N. Herrmann, C. Heyn, I. Aubert, A. Boutet, et al., Blood-brain barrier opening in Alzheimer's disease using MR-guided focused ultrasound, *Nature Commun.* 9 (1) (2018) 2336.
- [8] P. Anastasiadis, J.A. Winkles, A.J. Kim, G.F. Woodworth, Focused ultrasound-mediated blood-brain barrier disruption for enhanced drug delivery to brain tumors, in: *Nanotherapy for Brain Tumor Drug Delivery*, Springer, 2021, pp. 205–223.

- [9] K.T. Chen, K.C. Wei, H.L. Liu, Theranostic strategy of focused ultrasound induced blood-brain barrier opening for CNS disease treatment, *Front. Pharmacol.* 10 (FEB) (2019) <http://dx.doi.org/10.3389/fphar.2019.00086>.
- [10] R.D. Airan, R.A. Meyer, N.P. Ellens, K.R. Rhodes, K. Farahani, M.G. Pomper, S.D. Kadam, J.J. Green, Noninvasive targeted transcranial neuromodulation via focused ultrasound gated drug release from nanoemulsions, *Nano Lett.* 17 (2) (2017) 652–659.
- [11] J.B. Wang, M. Aryal, Q. Zhong, D.B. Vyas, R.D. Airan, Noninvasive ultrasonic drug uncaging maps whole-brain functional networks, *Neuron* 100 (3) (2018) 728–738.
- [12] H. Lea-Banks, Y. Meng, S.-K. Wu, R. Belhadjhamida, C. Hamani, K. Hynynen, Ultrasound-sensitive nanodroplets achieve targeted neuromodulation, *J. Control. Release* (2021).
- [13] H. Lea-Banks, M.A. O'Reilly, K. Hynynen, Ultrasound-responsive droplets for therapy: A review, *J. Control. Release* 293 (November 2018) (2019) 144–154, <http://dx.doi.org/10.1016/j.jconrel.2018.11.028>.
- [14] J. Kubanek, Neuromodulation with transcranial focused ultrasound, *Neurosurg. Focus* 44 (2) (2018) E14.
- [15] W.J. Tyler, S.W. Lani, G.M. Hwang, Ultrasonic modulation of neural circuit activity, *Curr. Opin. Neurobiol.* 50 (2018) 222–231.
- [16] J. Blackmore, S. Shrivastava, J. Sallet, C.R. Butler, R.O. Cleveland, Ultrasound neuromodulation: A review of results, mechanisms and safety, *Ultrasound Med. Biol.* 45 (7) (2019) 1509–1536.
- [17] J. Kubanek, J. Brown, P. Ye, K.B. Pauly, T. Moore, W. Newsome, Remote, brain region-specific control of choice behavior with ultrasonic waves, *Sci. Adv.* 6 (21) (2020) eaaz4193.
- [18] J.L. Sanguinetti, S. Hameroff, E.E. Smith, T. Sato, C.M. Daft, W.J. Tyler, J.J. Allen, Transcranial focused ultrasound to the right prefrontal cortex improves mood and alters functional connectivity in humans, *Front. Hum. Neurosci.* 14 (2020) 52.
- [19] B.W. Badran, K.A. Caulfield, S. Stomberg-Firestein, P.M. Summers, L.T. Dowdle, M. Savoca, X. Li, C.W. Austelle, E.B. Short, J.J. Borckardt, et al., Sonication of the anterior thalamus with MRI-guided transcranial focused ultrasound (tFUS) alters pain thresholds in healthy adults: A double-blind, sham-controlled study, *Brain Stimul.* 13 (6) (2020) 1805–1812.
- [20] L. Verhagen, C. Gallea, D. Folloni, C. Constans, D.E. Jensen, H. Ahnine, L. Roumazeilles, M. Santin, B. Ahmed, S. Lehéry, et al., Offline impact of transcranial focused ultrasound on cortical activation in primates, *Elife* 8 (2019) e40541.
- [21] E.F. Fouragnan, B.K. Chau, D. Folloni, N. Kolling, L. Verhagen, M. Klein-Flügge, L. Tankelevitch, G.K. Papageorgiou, J.-F. Aubry, J. Sallet, et al., The macaque anterior cingulate cortex translates counterfactual choice value into actual behavioral change, *Nature Neurosci.* 22 (5) (2019) 797–808.
- [22] N. Khalighinejad, A. Bongioanni, L. Verhagen, D. Folloni, D. Attali, J.-F. Aubry, J. Sallet, M.F. Rushworth, A basal forebrain-cingulate circuit in macaques decides it is time to act, *Neuron* 105 (2) (2020) 370–384.
- [23] V. Velling, S. Shklyaruk, Modulation of the functional state of the brain with the aid of focused ultrasonic action, *Neurosci. Behav. Physiol.* 18 (5) (1988) 369–375.
- [24] R.F. Dallapiazza, K.F. Timbie, S. Holmberg, J. Gatesman, M.B. Lopes, R.J. Price, G.W. Miller, W.J. Elias, Noninvasive neuromodulation and thalamic mapping with low-intensity focused ultrasound, *J. Neurosurg.* (2017) 1–10.
- [25] A. Fomenko, C. Neudorfer, R.F. Dallapiazza, S.K. Kalia, A.M. Lozano, Low-intensity ultrasound neuromodulation: An overview of mechanisms and emerging human applications, *Brain Stimul.* (2018).
- [26] W.S. Chang, H.H. Jung, E. Zadicario, I. Rachmilevitch, T. Tlusty, S. Vitek, J.W. Chang, Factors associated with successful magnetic resonance-guided focused ultrasound treatment: efficiency of acoustic energy delivery through the skull, *J. Neurosurg.* 124 (2) (2016) 411–416.
- [27] J.K. Mueller, L. Ai, P. Bansal, W. Legon, Numerical evaluation of the skull for human neuromodulation with transcranial focused ultrasound, *J. Neural Eng.* 14 (6) (2017) 066012.
- [28] H. Chen, E.E. Konofagou, The size of blood-brain barrier opening induced by focused ultrasound is dictated by the acoustic pressure, *J. Cereb. Blood Flow Metab.* 34 (7) (2014) 1197–1204.
- [29] W. Lee, H.-C. Kim, Y. Jung, Y.A. Chung, I.-U. Song, J.-H. Lee, S.-S. Yoo, Transcranial focused ultrasound stimulation of human primary visual cortex, *Sci. Rep.* 6 (2016).
- [30] V. Braun, J. Blackmore, R.O. Cleveland, C.R. Butler, Transcranial ultrasound stimulation in humans is associated with an auditory confound that can be effectively masked, *Brain Stimul.* 13 (6) (2020) 1527–1534.
- [31] M. Plaksin, E. Kimmel, S. Shoham, Cell-type-selective effects of intramembrane cavitation as a unifying theoretical framework for ultrasonic neuromodulation, *Eneuro* 3 (3) (2016).
- [32] A.Y. Ammi, T.D. Mast, I.-H. Huang, T.A. Abruzzo, C.-C. Coussios, G.J. Shaw, C.K. Holland, Characterization of ultrasound propagation through ex-vivo human temporal bone, *Ultrasound Med. Biol.* 34 (10) (2008) 1578–1589.
- [33] S. Purkayastha, F. Sorond, Transcranial Doppler ultrasound: technique and application, *Semin. Neurol.* 32 (4) (2012) 411.

- [34] Z. Wang, T. Komatsu, H. Mitsumura, N. Nakata, T. Ogawa, Y. Iguchi, M. Yokoyama, An uncovered risk factor of sonothrombolysis: substantial fluctuation of ultrasound transmittance through the human skull, *Ultrasonics* 77 (2017) 168–175.
- [35] D.E. Soulioti, D. Espindola, P.A. Dayton, G.F. Pinton, Super-resolution imaging through the human skull, *IEEE Trans. Ultrason. Ferroelectr. Freq. Control* 67 (1) (2019) 25–36.
- [36] S.T. Brinker, F. Preiswerk, P.J. White, T.Y. Mariano, N.J. McDannold, E.J. Bublrick, Focused ultrasound platform for investigating therapeutic neuromodulation across the human hippocampus, *Ultrason. Med. Biol.* 46 (5) (2020) 1270–1274, <http://dx.doi.org/10.1016/j.ultrasmedbio.2020.01.007>.
- [37] W. Legon, T.F. Sato, A. Opitz, J. Mueller, A. Barbour, A. Williams, W.J. Tyler, Transcranial focused ultrasound modulates the activity of primary somatosensory cortex in humans, *Nature Neurosci.* 17 (2) (2014) 322–329.
- [38] W. Lee, H. Kim, Y. Jung, I.-U. Song, Y.A. Chung, S.-S. Yoo, Image-guided transcranial focused ultrasound stimulates human primary somatosensory cortex, *Sci. Rep.* 5 (2015).
- [39] W. Legon, L. Ai, P. Bansal, J.K. Mueller, Neuromodulation with single-element transcranial focused ultrasound in human thalamus, *Hum. Brain Mapp.* 39 (5) (2018) 1995–2006.
- [40] W. Legon, P. Bansal, R. Tyshynsky, L. Ai, J.K. Mueller, Transcranial focused ultrasound neuromodulation of the human primary motor cortex, *Sci. Rep.* 8 (1) (2018) 1–14.
- [41] F.J. Fry, J.E. Barger, Acoustical properties of the human skull, *J. Acoust. Soc. Am.* 63 (5) (1978) 1576–1590.
- [42] P.J. White, G.T. Clement, K. Hynynen, Longitudinal and shear mode ultrasound propagation in human skull bone, *Ultrason. Med. Biol.* 32 (7) (2006) 1085–1096.
- [43] S. Pichardo, V.W. Sin, K. Hynynen, Multi-frequency characterization of the speed of sound and attenuation coefficient for longitudinal transmission of freshly excised human skulls, *Phys. Med. Biol.* 56 (1) (2010) 219.
- [44] S. Pichardo, C. Moreno-Hernández, R.A. Drainville, V. Sin, L. Curiel, K. Hynynen, A viscoelastic model for the prediction of transcranial ultrasound propagation: application for the estimation of shear acoustic properties in the human skull, *Phys. Med. Biol.* 62 (17) (2017) 6938.
- [45] F. Fry, Transkull transmission of an intense focused ultrasonic beam, *Ultrason. Med. Biol.* 3 (2–3) (1977) 179–184.
- [46] J.E. Barger, Attenuation and dispersion of ultrasound in cancellous bone, *Ultrason. Tissue Charact.* 11 (1979) 197–201.
- [47] J. Evans, M. Tavakoli, Ultrasonic attenuation and velocity in bone, *Phys. Med. Biol.* 35 (10) (1990) 1387.
- [48] M. Tavakoli, J. Evans, Dependence of the velocity and attenuation of ultrasound in bone on the mineral content, *Phys. Med. Biol.* 36 (11) (1991) 1529.
- [49] G. Clement, K. Hynynen, Correlation of ultrasound phase with physical skull properties, *Ultrason. Med. Biol.* 28 (5) (2002) 617–624.
- [50] G. Pinton, J.-F. Aubry, E. Bossy, M. Muller, M. Pernot, M. Tanter, Attenuation, scattering, and absorption of ultrasound in the skull bone, *Med. Phys.* 39 (1) (2012) 299–307.
- [51] K. Hynynen, J. Sun, Trans-skull ultrasound therapy: the feasibility of using image-derived skull thickness information to correct the phase distortion, *IEEE Trans. Ultrason. Ferroelectr. Freq. Control* 46 (3) (1999) 752–755.
- [52] J. Aarnio, G.T. Clement, K. Hynynen, A new ultrasound method for determining the acoustic phase shifts caused by the skull bone, *Ultrason. Med. Biol.* 31 (6) (2005) 771–780.
- [53] P. White, G. Clement, K. Hynynen, Local frequency dependence in transcranial ultrasound transmission, *Phys. Med. Biol.* 51 (9) (2006) 2293.
- [54] L. Marsac, D. Chauvet, R. La Greca, A.-L. Boch, K. Chaumoitre, M. Tanter, J.-F. Aubry, Ex vivo optimisation of a heterogeneous speed of sound model of the human skull for non-invasive transcranial focused ultrasound at 1 MHz, *Int. J. Hyperther.* 33 (6) (2017) 635–645.
- [55] T.D. Webb, S.A. Leung, J. Rosenberg, P. Ghanouni, J.J. Dahl, N.J. Pelc, K.B. Pauly, Measurements of the relationship between CT Hounsfield units and acoustic velocity and how it changes with photon energy and reconstruction method, *IEEE Trans. Ultrason. Ferroelectr. Freq. Control* 65 (7) (2018) 1111–1124.
- [56] S.A. Leung, T.D. Webb, R.R. Bitton, P. Ghanouni, K.B. Pauly, A rapid beam simulation framework for transcranial focused ultrasound, *Sci. Rep.* 9 (1) (2019) 1–11.
- [57] L. Deng, A. Hughes, K. Hynynen, A noninvasive ultrasound resonance method for detecting skull induced phase shifts may provide a signal for adaptive focusing, *IEEE Trans. Biomed. Eng.* 67 (9) (2020) 2628–2637.
- [58] A.Y. Ammi, T.D. Mast, I.-H. Huang, T.A. Abruzzo, C.-C. Coussios, G.J. Shaw, C.K. Holland, Characterization of ultrasound propagation through ex-vivo human temporal bone, *Ultrason. Med. Biol.* 34 (10) (2008) 1578–1589, <http://dx.doi.org/10.1016/j.ultrasmedbio.2008.02.012>.
- [59] M.A. Phipps, S.V. Jonathan, P.F. Yang, V. Chaplin, L.M. Chen, W.A. Grissom, C.F. Caskey, Considerations for ultrasound exposure during transcranial MR acoustic radiation force imaging, *Sci. Rep.* 9 (1) (2019) 1–11, <http://dx.doi.org/10.1038/s41598-019-52443-8>.
- [60] M.D. Eames, A. Hananel, J.W. Snell, N.F. Kassell, J.F. Aubry, Trans-cranial focused ultrasound without hair shaving: Feasibility study in an ex vivo cadaver model, *J. Ther. Ultrasound* 1 (1) (2014) 2–7, <http://dx.doi.org/10.1186/2050-5736-1-24>.
- [61] S.L. Alexander, K. Rafaels, C.A. Gunnarsson, T. Weerasooriya, Structural analysis of the frontal and parietal bones of the human skull, *J. Mech. Behav. Biomed. Mater.* 90 (November 2018) (2019) 689–701, <http://dx.doi.org/10.1016/j.jmbbm.2018.10.035>.
- [62] M. Crocco, P. Pellegretti, C. Sciallero, A. Trucco, Combining multi-pulse excitation and chirp coding in contrast-enhanced ultrasound imaging, *Meas. Sci. Technol.* 20 (10) (2009) 104017.
- [63] S. Callegari, M. Ricci, S. Caporale, M. Monticelli, M. Erolu, L. Senni, R. Rovatti, G. Setti, P. Burrascano, From chirps to random-FM excitations in pulse compression ultrasound systems, in: *2012 IEEE International Ultrasonics Symposium, IEEE*, 2012, pp. 471–474.
- [64] J.-F. Aubry, M. Tanter, M. Pernot, J.-L. Thomas, M. Fink, Experimental demonstration of noninvasive transskull adaptive focusing based on prior computed tomography scans, *J. Acoust. Soc. Am.* 113 (1) (2003) 84–93, <http://dx.doi.org/10.1121/1.1529663>.
- [65] N. Lynnerup, Cranial thickness in relation to age, sex and general body build in a Danish forensic sample, *Forensic Sci. Int.* 117 (1–2) (2001) 45–51, [http://dx.doi.org/10.1016/S0379-0738\(00\)00447-3](http://dx.doi.org/10.1016/S0379-0738(00)00447-3).
- [66] N. Lynnerup, J.G. Astrup, B. Sejrsen, Thickness of the human cranial diploe in relation to age, sex and general body build, *Head Face Med.* 1 (2005) 13, <http://dx.doi.org/10.1186/1746-160x-1-13>.
- [67] H.H. De Boer, A.E. Van der Merwe, V.V. Soerdjbalie-Maikoe, Human cranial vault thickness in a contemporary sample of 1097 autopsy cases: relation to body weight, stature, age, sex and ancestry, *Int. J. Legal Med.* 130 (5) (2016) 1371–1377, <http://dx.doi.org/10.1007/s00414-016-1324-5>.
- [68] Acoustic attenuation: Multifrequency measurement and relationship to CT and MR imaging, *IEEE Trans. Ultrason. Ferroelectr. Freq. Control* 68 (5) (2021) 1532–1545, <http://dx.doi.org/10.1109/TUFFC.2020.3039743>.
- [69] G.W. Miller, M. Eames, J. Snell, J.-F. Aubry, Ultrashort echo-time MRI versus CT for skull aberration correction in MR-guided transcranial focused ultrasound: In vitro comparison on human calvaria, *Med. Phys.* 42 (5) (2015) 2223–2233.



Thomas S. Riis received the B.A. degree in applied mathematics and the B.A. degree in physics from University of California, Berkeley, CA, USA, in 2016. He is currently pursuing the Ph.D. degree in biomedical engineering at the University of Utah, Salt Lake City, UT, USA. He joined the Allen Institute for Brain Science in 2016, where he worked on electrophysiological recordings and optogenetic stimulation of cortex in mice. In 2018, he joined Dr. Jan Kubanek's laboratory, University of Utah, where he works on developing new ways to modulate the nervous system noninvasively and in a targeted manner.



Taylor D. Webb received the B.S. degree and the M.S. degree in electrical engineering from Brigham Young University (BYU), Provo, UT, USA in 2010 and 2012, respectively, and the Ph.D. degree from Stanford University, Stanford, CA, USA, in 2019. He is currently working as a Postdoctoral Fellow at the University of Utah, where he is applying transcranial neuromodulatory ultrasound to deep brain targets of awake behaving monkeys.



Jan Kubanek is an Assistant Professor in Biomedical Engineering at the University of Utah. He received his Ph.D. in Biomedical Engineering from Washington University in 2013. His lab, which comprises four PhD students and one postdoc, is funded by the NIH and private foundations. The goal of the lab is to develop neuromodulation approaches that are noninvasive, focal, and act at depth, so that we can provide treatment options to the many patients with treatment-resistant disorders of brain function.